

Article

Ultraviolet-Sensor Based on Tin-Doped Zinc Oxide Thin Films Grown by Spray Pyrolysis

Matías Valdés , Edgar A. Villegas , Leandro A. Ramajo  and Rodrigo Parra

Instituto de Investigaciones en Ciencia y Tecnología de Materiales (INTEMA), Facultad de Ingeniería, Universidad Nacional de Mar del Plata—Consejo de Investigaciones Científicas y Técnicas (CONICET), Mar del Plata 7600, Argentina; edgarvillegas5@gmail.com (E.A.V.); lramajo@fi.mdp.edu.ar (L.A.R.); rparra@fi.mdp.edu.ar (R.P.)

* Correspondence: mvaldes@fi.mdp.edu.ar

Abstract: The development of sensors that can monitor ultraviolet radiation has many implications for daily life, and even more so if the focus is on low-cost solution processes and the use of eco-friendly materials. In this study, we produced a UV-sensor based on Sn-doped ZnO thin films grown by spray pyrolysis, with a doping content ranging from 1 to 10 at.%. The study focuses on the characterization of the films and the device, and their potential for UV detection. Structural analysis via XRD, FESEM, and STEM confirms the polycrystalline nature of the films, with a hexagonal single-phase wurtzite structure of ZnO. Although the dopant content in the films was widely varied, optoelectronic properties such as transmittance, resistivity, energy gap, density, and carrier mobility are not significantly modified. Sprayed Sn-doped ZnO films demonstrated high sensitivity to ultraviolet light, whether monochromatic or that coming from solar radiation. Outdoor measurements showed promising performance of the UV-sensor, indicating its potential applicability for real-time UV monitoring and potential use. Overall, sprayed Sn-doped ZnO thin films offer a viable and low-cost solution for the fabrication of UV-sensors with desirable properties such as a wide and direct bandgap, high sensitivity, and ease of fabrication.

Keywords: UV; sensor; thin films; spray pyrolysis; doping; ZnO



Citation: Valdés, M.; Villegas, E.A.; Ramajo, L.A.; Parra, R.

Ultraviolet-Sensor Based on Tin-Doped Zinc Oxide Thin Films Grown by Spray Pyrolysis. *Ceramics* **2024**, *7*, 1500–1512. <https://doi.org/10.3390/ceramics7040097>

Academic Editors: Kamalan Kirubakaran Amirtharaj Mosas and Doni Daniel

Received: 16 August 2024
Revised: 4 October 2024
Accepted: 8 October 2024
Published: 14 October 2024



Copyright: © 2024 by the authors. Licensee MDPI, Basel, Switzerland. This article is an open access article distributed under the terms and conditions of the Creative Commons Attribution (CC BY) license (<https://creativecommons.org/licenses/by/4.0/>).

1. Introduction

Since its discovery in 1801, ultraviolet (UV) radiation has been recognized as a significant constituent of solar radiation [1]. Despite constituting less than 10% of the total solar radiation, UV radiation exerts a profound influence on human survival and development [2,3]. For instance, moderate exposure of the skin to natural or artificial UV light offers health benefits, such as aiding in the synthesis of Vitamin D, germicidal effects, and the prevention or treatment of rickets. Conversely, excessive UV radiation can lead to various ailments, including cataracts, skin cancer, and accelerated aging [2]. Furthermore, UV radiation strongly impacts crop yields and the longevity of buildings [4,5]. Therefore, UV radiation detection and monitoring have become almost mandatory to protect human health, promote sun safety, and prevent skin cancer [6], as well as monitor environmental conditions [4], and optimize industrial processes [7].

UV radiation is divided into three categories: UVA (320–400 nm), UVB (290–320 nm), and UVC (100–290 nm). UVC is absorbed by the atmosphere, while UVA and UVB reach the Earth's surface. UVA, making up 95% of UV radiation, penetrates deeper into the skin and contributes to aging and cell damage [3]. UVB is more energetic and linked to sunburn and skin cancer. The World Health Organization (WHO) considers exposure above 3 mW/cm² of UVB to be harmful, highlighting the need for UV radiation monitoring [5].

Knowing the levels of UV radiation provides valuable information for decision-making, awareness, and the implementation of appropriate measures to mitigate the potential risks associated with UV radiation exposure. Recently, there has been a lot of

interest in incorporating sensors into wearable devices or embedding them in smartphone apps to provide real-time UV index readings [6,8–10]. This allows people to make informed decisions about sun protection measures, such as using sunscreen, wearing protective clothing and hats, or seeking shade during peak UV hours. By providing personalized information about UV exposure, these sensors help individuals adopt sun-safe behaviors and reduce the risk of UV-related health problems. The fabrication of UV-sensors for outdoor conditions presents significant challenges, particularly in ensuring accuracy and sensitivity to UV radiation amidst environmental factors such as temperature fluctuations and the presence of a broad light spectrum. These sensors must distinguish UV radiation from visible and infrared light, making their design more complex [9–11]. Furthermore, for outdoor applications, conventional “UV-enhanced” silicon photodiodes face several drawbacks [12]. Silicon absorbs light in both the visible and infrared regions due to its narrow bandgap energy (1.1 eV at room temperature). Although filters can block out visible and infrared photons, this causes a significant loss of effective area for the instrument. Additionally, for high-sensitivity applications, the active area of the detector must be cooled to reduce dark current [12]. Solid-state detectors made of wide bandgap materials such as GaN, ZnSe, AlGaN, diamond, ZnO, etc., exhibit high performance for UV detection [11,13,14].

A wide and direct bandgap structure (3.37 eV at ambient temperature), a large exciton binding energy (60 meV), and thermal stability are just a few of the many benefits of ZnO as a semiconductor material. In addition to being inexpensive and non-toxic, ZnO can be deposited as a thin film using methods that do not require a vacuum or very high deposition temperatures. However, the fabrication of ZnO p-n junction-based UV-sensor devices is not feasible due to the challenge of p-type doping in ZnO [15,16]. Therefore, ZnO detectors in through-beam are very efficient in UV detection due to their very fast response and low noise level, making them an ideal candidate for UV-monitoring.

To achieve a true cost reduction, non-vacuum and soft chemistry techniques present very attractive characteristics for obtaining semiconductor thin films and devices. Spray pyrolysis is an adaptable technique that has been used to deposit many different compounds and is considered a low-cost technique compared to physical vapor deposition (PVD) methods primarily due to its simplicity in equipment and operational requirements [17]. It typically involves basic components such as spray nozzles and heating substrates, without the need for high-vacuum systems or intricate infrastructure [18]. Additionally, the process can be conducted in ambient conditions, further reducing costs associated with complex control environments. This simplicity makes spray pyrolysis cost-effective, especially for large-area film deposition [17,18].

In this work, we present Sn-doped ZnO films obtained by Spray Pyrolysis that are designed and characterized for the fabrication of UV-sensors. Our films not only demonstrate high sensitivity to monochromatic UV light but are also responsive to broad-spectrum sources such as solar simulators. Promising results are also observed from real outdoor measurements conducted as a pilot test for integrating these films into a UV-sensor.

2. Materials and Methods

Tin-doped zinc oxide (TZO, Sn:ZnO) films were grown by Spray Pyrolysis on microscope slide ($70 \times 25 \text{ mm}^2$). In a previous step, a 100 nm SiO₂ coating was deposited on the glass slides as a barrier layer against the diffusion of alkali ions that can interfere in the electrical response of the sensor. For this, 40 mL of 2-propanol were used to dissolve 10 mL of tetraethoxysilane (TEOS 98%, Sigma-Aldrich, Merck KGaA, Darmstadt, Germany). The TEOS solution was then mixed with 3.5 mL of a 4.2% nitric acid aqueous solution. Glass microscope slides were dip-coated in the resultant sol at a speed of 3 cm/min. Coated substrates were heat-treated in a furnace at 450 °C for 40 min with heating and cooling rates of 3 °C/min in order to densify the silica film and enhance its barrier capabilities against the migration of alkaline ions from the glass substrate to the active film. The thickness of the SiO₂ barrier layer is around 180 nm (see Figure S1, Supplementary Materials).

Later, TZO films were deposited, spraying 0.5 mol/L Zn^{+2} solution via dissolution of $\text{Zn}(\text{OCOCH}_3)_2 \cdot 2\text{H}_2\text{O}$ (98%, Cicarelli, San Lorenzo, Santa Fe, Argentina) in ethanol with the addition of acetylacetone (Acac, 99%, Sigma-Aldrich, Merck KGaA, Darmstadt, Germany) in a 1:1 Zn:Acac molar ratio. For doping, a 0.1 mol/L SnC_2O_4 (tin(II) oxalate, 98% Sigma-Aldrich, Merck KGaA, Darmstadt, Germany) solution was added to the zinc solution in different volumetric ratios to achieve nominal doping concentrations from 1% to 10% of Sn in TZO films. The solution was sprayed onto the glass substrates at 425 °C with nitrogen (1.5 bar) as a carrier gas at a nozzle–substrate distance of 15 cm.

Grazing incidence-X-ray diffraction (GI-XRD) at 0.5° was employed to study the phase composition of TZO films with a PANalytical X'Pert diffractometer (Malvern-Panalytical, Malvern, UK) running with $\text{K}\alpha$ -Cu radiation. XRD patterns were compared with those in the standard crystallographic databases provided by the International Centre for Diffraction Data (ICDD) [19]. The microstructure and morphology of the films were examined using scanning electron microscopy (FE-SEM) in a FEI Quanta 250 FEG microscope (FEI, Hillsboro, OR, USA). High-resolution transmission electron microscopy images were obtained using a Thermo Scientific Talos F200X STEM (Thermo Fisher Scientific Fisher, Waltham, MA, USA). Optical transmittance was measured on the basis of UV–Visible spectra recorder with a UV–VIS–NIR Shimadzu 3600 spectrophotometer (Shimadzu Corp., Kyoto, Japan), equipped with an integrating sphere, in the 3600–200 nm range. The optical band gaps (E_g) were estimated from Tauc plots as the intersection of the linear fit of the region associated with the optical absorption edge with the energy axis [20,21]. Film thicknesses (t) were determined via mechanical profilometry with a KLA Tencor E-100 instrument (KLA, Milpitas, CA, USA). The sheet resistance (R_{sh}) measurements of TZO films were carried out with a SIGLENT SPD 3303D voltage source (SIGLENT TECH., Solon, OH, USA) coupled to a RIGOL 3062 digital multimeter (RIGOL, Portland, OR, USA) in Van der Paw configuration. From these measurements, the resistivity (ρ) of each TZO film was calculated according to the following expression:

$$\rho = R_{sh} \times t, \quad (1)$$

Carrier density (n) and mobility (μ) were determined using a home-built Hall effect system.

In a first approach, the pure UV response of TZO films was assessed under the illumination of two Philips UVA-region tube lamps of 365 nm maximum wavelength (340–400 nm spectral emission) and 4 W nominal power (2.5 mWcm^{-2} measured on film surface). A 4-lead sample holder and a chopper completed the measuring set-up. Rigol DM3058 and DM3062 digital multimeters were used in order to register the current–time response during several dark and light cycles of 60 s each, while a 10 V dc voltage was applied between probes.

As more oriented approaches to a sensor prototype, the photoresponse of TZO films was tested under simulated and real sunlight conditions (outdoor measurements). To reduce the intensity of the light neutral density (ND), filters were placed to reduce the light power of the solar simulator, simulating different solar radiation conditions during the day. Light output was measured with a Gentec Maestro power meter and UP19K-15S-H5 pyranometer (Gentec Electro-Optics, Inc., Quebec, Canada). Figure 1 shows the experimental setup employed for indoor and outdoor measurements at INTEMA location. These measurements were made at different times of the day to expose the films at different values of solar radiation. Again, the sun's radiation was measured with the pyranometer pointed directly at the sun with the same orientation used during indoor measurements. The photocurrent–time response was computed using an Ivium Compactstat potentiostat (Ivium Technologies B.V., Eindhoven, The Netherlands).

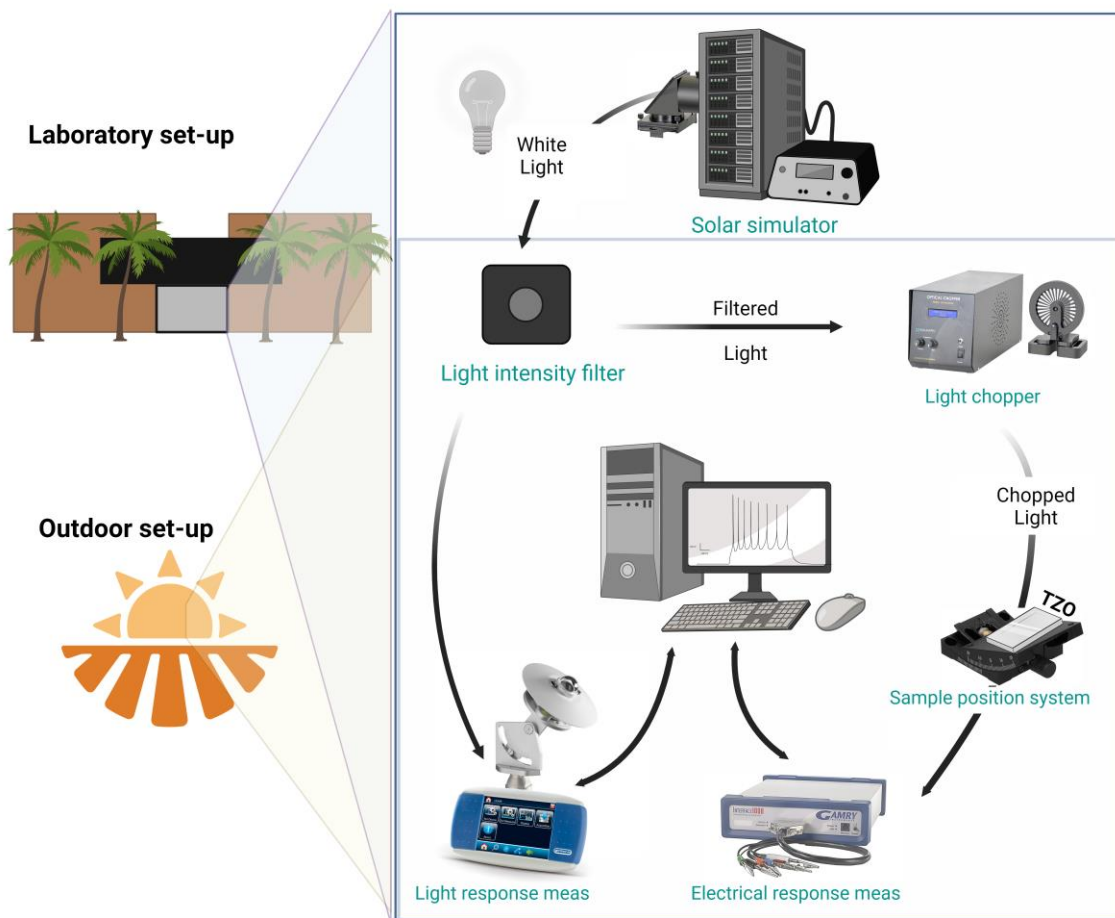


Figure 1. Experimental setup for outdoor testing of the UV-sensor at INTEMA location.

3. Results and Discussion

3.1. Structural Analysis

Figure 2 presents the X-ray diffraction of Sn-doped zinc oxide (TZO) films for different dopant contents. The XRD patterns reveal that the TZO films are polycrystalline with a single-phase structure, specifically identified as the wurtzite phase of zinc oxide (ZnO), in agreement with the JCPDS PDF 36-1451 (included in the figure for the sake of the comparison). Peaks labeled with an asterisk are produced by unfiltered $k\beta$ radiation of the X-ray Cu source. The diffraction peaks observed in the XRD patterns correspond to the crystallographic planes of the TZO film. Compared to the reference JCPDS file for a (not oriented) powder sample of ZnO, our films present diffraction peaks with different relative intensities. In particular, the peak (002) appears to be of greater intensity compared to the main peak (101) of the JCPDS file. This is due to the anisotropic growth of the crystal in the a and b directions, perpendicular to the c ([001]) direction. In agreement with a previous work on ZnO films [22], the oxide has crystallized in the form of grains similar to hexagonal platelets, showing mainly (001) faces, instead of elongated structures or rods with a hexagonal cross section [23]. Notably, there is a slight shift towards lower 2θ values for the (101) and higher angles for the (002) peaks, respectively, attributed to a lattice strain within the films. This peak shift can be also linked to the difference in ionic radii between Sn^{+4} (55 pm) and Zn^{+2} (60 pm) ions, and it has been observed not only in films doped with tin [24] but also with other elements such as aluminum [25,26] and indium [27]. Thus, the XRD analysis confirms the crystalline nature of the TZO films and provides information about the crystal structure and grain morphology. Figure 3 presents structural characteristics of sprayed TZO thin films for different doping percentages. Figure 3a–c shows SEM images of the TZO thin films for different doping contents, which enable an

examination of its morphological characteristics and surface topography. In this way, SEM images reveal the distinctive hexagonal shape of TZO crystals, which is frequently observed for zinc oxide films. Furthermore, the SEM images provide a clear visualization of the grain structure and distribution present within the film. In agreement with the analysis of the XRD patterns, the films are composed of bidimensional hexagonal grains exposing (001) faces. Analysis of these pictures with *ImageJ* software (1.54j, 12 June 2024) unveiled that the average grain size of the different TZO films is approximately 200 nm for the 1% doped film and 80 nm for 7% and 10% TZO films, showing that the segregation of the impurities at grain boundaries inhibits grain growth. The high degree of homogeneity facilitated the estimation of the average grain size through statistical analysis. This information provides valuable insights into the microstructure and grain boundaries of the film, which play pivotal roles in influencing its optical and electrical properties. A table with the thicknesses of the different TZO films determined via profilometry is presented as an insert in Figure 3. As can be seen, the average thickness of TZO is around 150 nm, which is obtained with only a 20 mL deposition of precursor solution. Some of the profilometry measurements are presented in Figure S1 of the Supplementary Materials. Figure 4 shows a high-resolution TEM image of the same 7% TZO film. The image reveals the typical crystalline structure of ZnO over an apparently defect-free region, with identifiable crystal planes according to the reference pattern in the JCPDS PDF 36-1451 file.

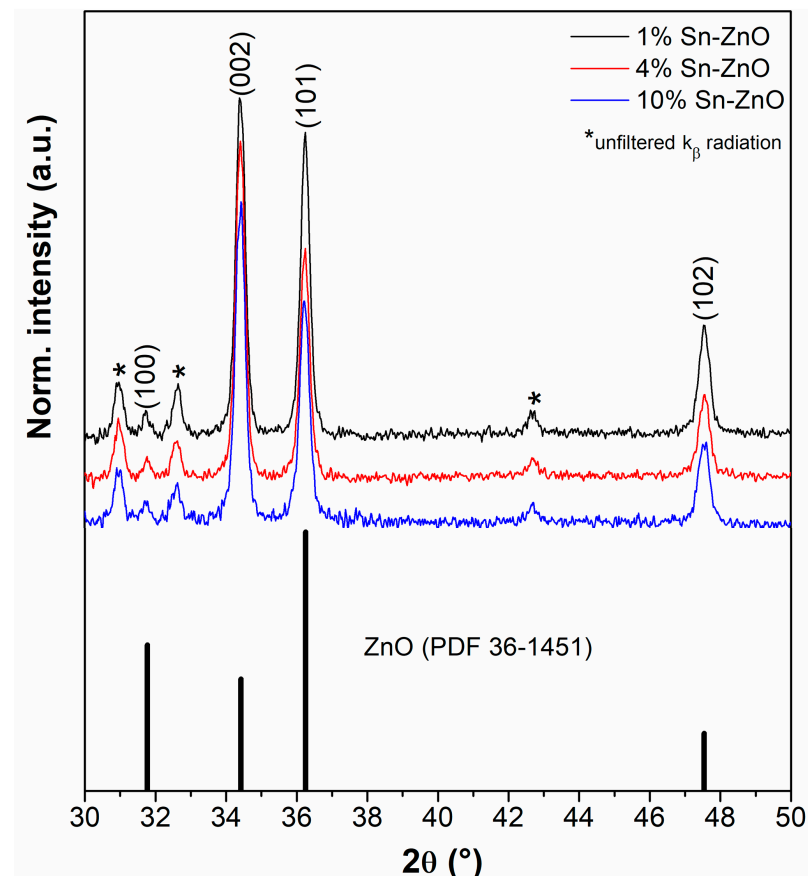


Figure 2. X-ray diffraction (XRD) patterns of selected TZO films and ZnO JCPDS PDF file 36-1451.

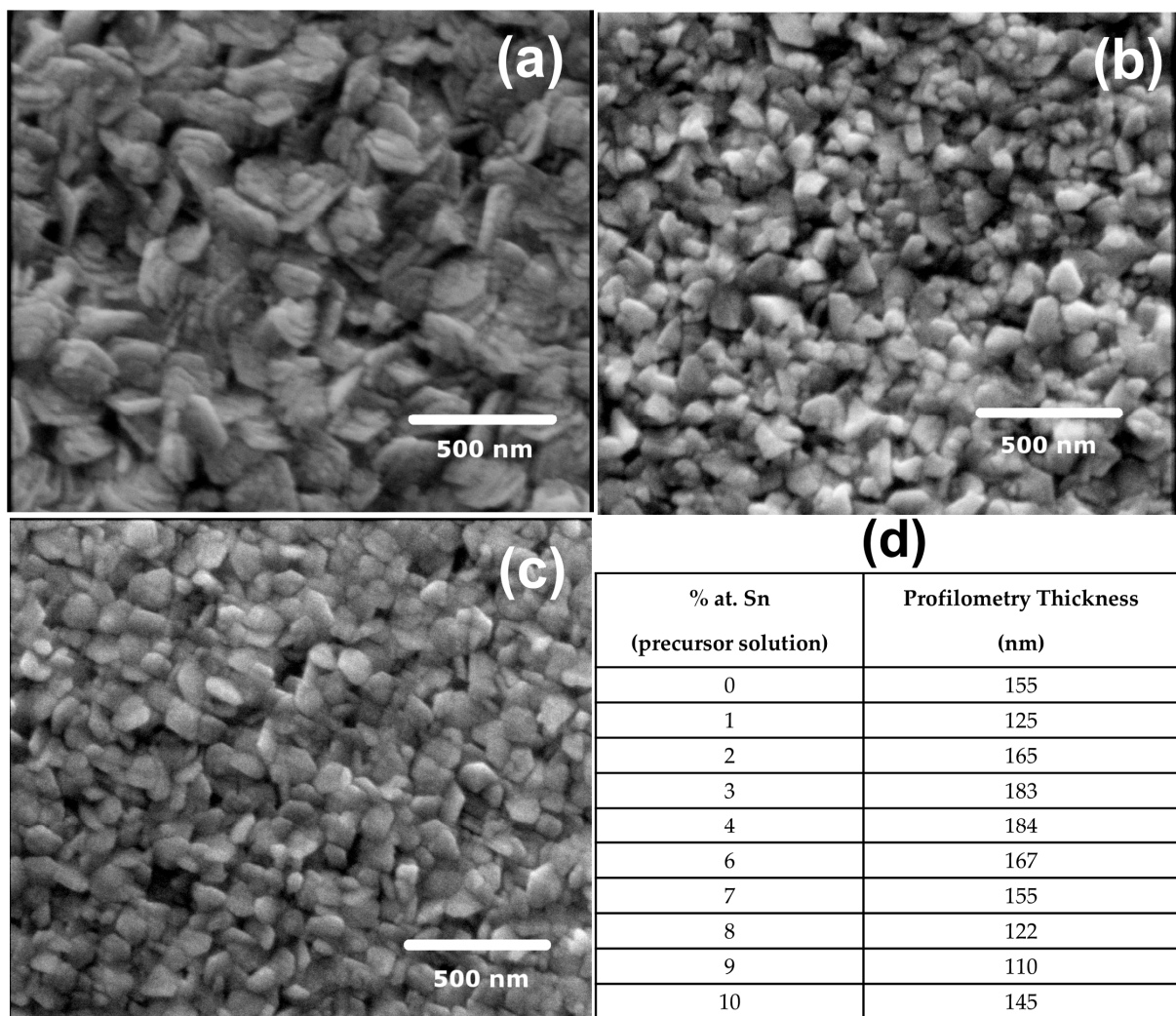


Figure 3. SEM surface images of (a) 1% Sn-doped, (b) 7% Sn-doped, and (c) 10% Sn-doped zinc oxide (TZO) sprayed films. (d) Table of TZO film thicknesses estimated by profilometry.

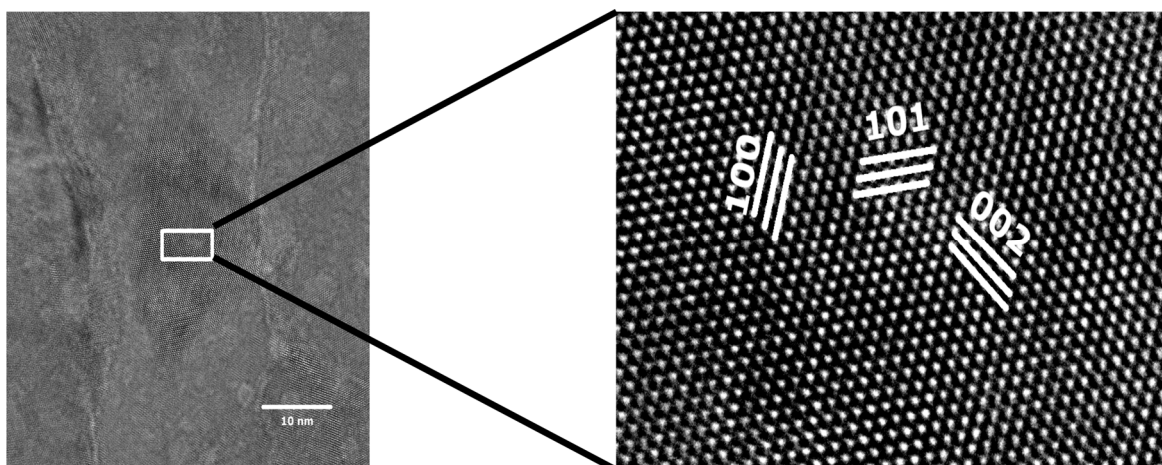


Figure 4. HR-TEM image of Sn-doped zinc oxide (7% TZO) thin film.

3.2. Electric and Optical Characterization

Figure 5a depicts the optical transmittance of TZO films where it can be observed a high transparency (~80% average) in the 400 to 1200 nm range, which is required for outdoors

UV-sensor to minimize the visible and IR interference during daylight measurements [6,11]. From the transmittance curves, the optical band-gap energy values (E_g) for each TZO film were estimated. Tauc graphs were used through the relationship $(\alpha h\nu)^m$ vs. $h\nu$, where $h\nu$ is the photon energy and the absorption coefficient α is obtained from transmittance T . The exponent m that must be chosen for the plot depends on the nature of the expected transition, being $m = 2$ for direct semiconductors such as ZnO. Figure 5b shows the E_g values obtained as a function of the tin content in each film. E_g values range between 3.3 and 3.2 eV, which are the values usually reported for ZnO films [28–30]. The effect of Sn doping on the band gap energy is a topic of ongoing discussion. Chahmat et al. bring up this matter in their work after observing an oscillating behavior of the E_g value of Sn-doped sprayed ZnO films that is comparable to what is observed in this work [31]. While certain phenomena contribute to band gap narrowing (BGN), others contribute to band gap widening (BGW) upon doping. Among the former we can mention many body interactions [32], or the creation of deep states by Sn^{+4} incorporation [33]; while BGW is mainly associated with the Burstein–Moss effect, which implies that optical band gap broadening occurs because lower states in the conduction band are blocked by doping [31,32,34]. The E_g values in Figure 5 do not present a clear trend, and this could be because none of the aforementioned phenomena manifest themselves or because there is some competition between them resulting in an oscillatory tendency of the energy gap.

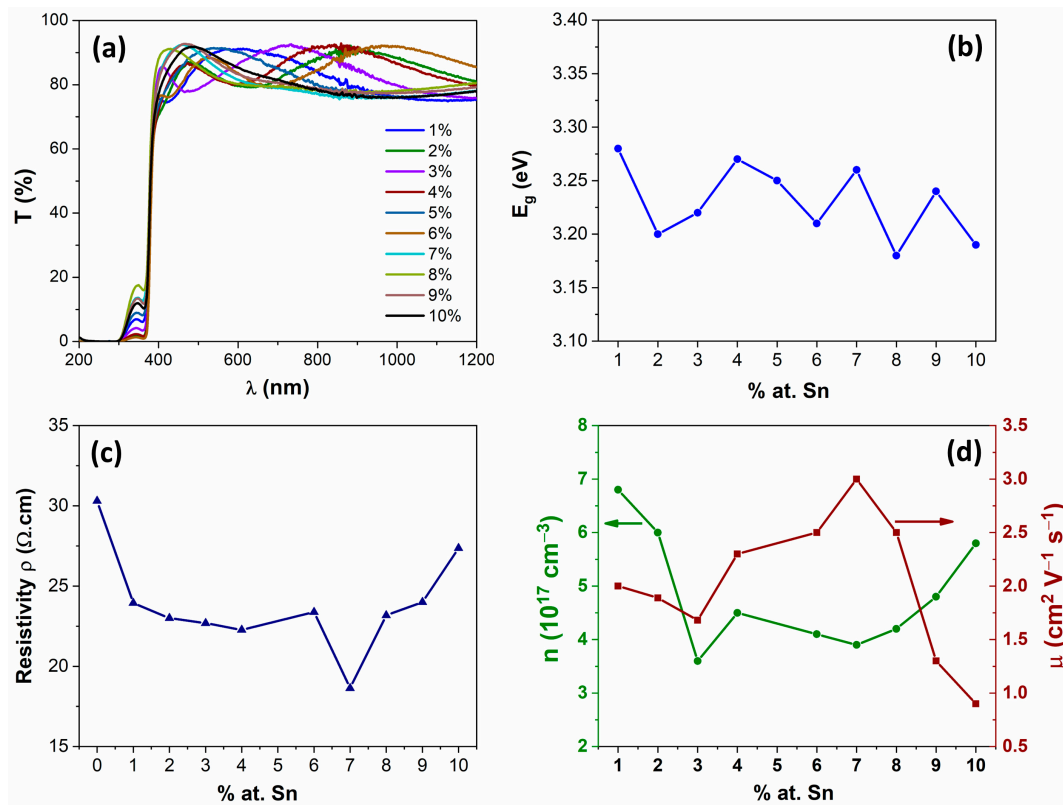


Figure 5. (a) Optical transmittance of TZO films; (b) energy gap (E_g) values of TZO films derived from the Tauc equation; (c) resistivity values of TZO films calculated from Van der Paw measurements; and (d) carrier density and electron mobility values of TZO films obtained from Hall effect.

In the range between 300 and 350 nm, a second peak can be observed in the transmittance spectra. We believe that this signal may be associated with a glass/ SiO_2 substrate effect. Indeed, SiO_2 exhibits a direct optical band gap around 3.5 eV [35]. The role of SiO_2 as a barrier layer was previously explained in the experimental section. Further studies are being performed to elucidate this contribution in the transmittance spectra.

Figure 5c presents the resistivity values (ρ) obtained using the sheet resistance (R_{sh}) and the film thickness (t) estimated using profilometry. The resistivity value decreases

with the addition of tin to the ZnO lattice. Despite a minimum resistivity below 20 $\Omega\cdot\text{cm}$ measured for the 7% Sn-ZnO film; 1–9% Sn-doped films showed an average resistivity of 23 $\Omega\cdot\text{cm}$. The charge carrier density (n) and electron mobility (μ) curves of the TZO films as a function of Sn doping are displayed in Figure 5d. The charge carrier mobility reaches a maximum at this minimal resistivity value, and the charge carrier density values are in the order of 10^{17} cm^{-3} . The low carrier concentrations of these TZO films might explain the absence of the Burstein–Moss effect. Carrier concentrations in the order of $10^{19}\text{--}10^{21}\text{ cm}^{-3}$ have been reported for doped ZnO films, where the Burstein–Moss effect has been observed [29,36].

3.3. UV Response

The response of 1, 4, 7, and 10% Sn-doped ZnO films under UV light ($\lambda \approx 365\text{ nm}$) is depicted in Figure 6a. The photoresponse curves reveal the same behavior of all films, with no significant changes in their profiles. The current increases under UV illumination and it tends to stabilize in a maximum photocurrent value (I_p). In the absence of light, the current decreases exponentially and reaches a minimum dark current (I_d) value. The rapid decay of the current to the initial dark current value suggests a quick reabsorption of oxygen at the grains surfaces [37]. In agreement with previous reports [20,30], among the Sn-doped films, the most resistive (10% TZO) showed the highest I_p/I_d value (3.3). Although this film is characterized by a relatively high donor density, it showed the lowest mobility. Therefore, small changes in the concentration of surface states induced by UV light and oxygen desorption have a significant effect on conductivity. On the other hand, the 7%-TZO film is the least resistive film, with the highest mobility of charge carriers but with lower I_p/I_d value (2.0). Despite the lower sensitivity of the latter, its relatively low resistivity makes it suitable for sensor devices. Highly resistive films imply dealing with very low currents, which may complicate the design of reliable sensor devices. In a previous work of the group [5], it was observed in undoped ZnO films under UV irradiation that as the grain size increased, the ratio of UV light conductivity to dark conductivity (I_p/I_d) decreased; that is, films with smaller grains exhibited a higher sensitivity compared to films with larger grains [5]. From the SEM images (Figure 3), it can be seen that low %Sn results in films with larger grains compared to TZO with higher dopant percentages (7% and 10%) where films formed with smaller grains are observed. As well as showing higher conductivity and electron mobility values, the fine-grained microstructure might also contribute to the better performance of the 7% TZO films.

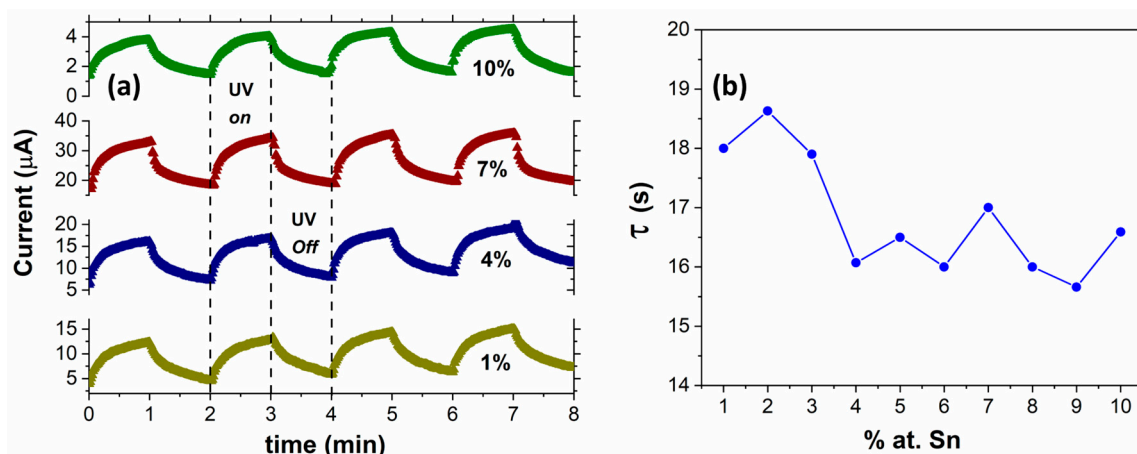


Figure 6. (a) UV-response of selected TZO films; (b) relaxation time (τ) of TZO films as a function of Sn content in the film.

The observed current decay was fitted using an exponential function of the form:

$$I(t) = I_d + (I_p - I_d) e^{-\frac{t}{\tau}}, \quad (2)$$

where I_p is the maximum current value when the film is exposed to UV light, I_d is the minimum current value in the dark, and τ is the relaxation time. The response of the TZO films fits well with this model, which only includes an exponential decay of the dark current associated with the reabsorption of oxygen at the surface, consistent with the previous work reported by Anhn et al. [38]. Other authors have added a second exponential decay attributed to water absorption in experimental conditions of high humidity (>65 HR) [30,39,40]. The relaxation time τ is related to the time necessary for the transition to occur from a state of maximum current to one of minimum current. This parameter is significant for establishing the suitability of the film for a UV-sensor. Additionally, the τ parameter indicates the speed of exchange phenomena on the surface, such as oxygen adsorption. For fast UV-sensors, the decay constant should be within 5τ . The values extracted from the fitting with Equation (2) are shown in Figure 6b.

A comparison between our research and the detection capabilities of TZO-based UV-sensors reported in the literature is presented in Table 1.

Table 1. Film thickness (d), visible transmittance (T_{vis}), optical band gap (E_g), carrier density (n), electron mobility (μ), resistivity (r), sensitivity (I_p/I_d), and decay time (t) for Sn-doped ZnO (TZO) films as reported in the literature.

TZO Composition	d (μm)	T_{vis} (%)	E_g (eV)	n (cm^{-3})	μ ($\text{cm}^2\text{V}^{-1}\text{s}^{-1}$)	r (W.cm)	I_p/I_d	t (s)	Reference
6% at. Sn-ZnO	0.65	88	3.24	N/A	N/A	648	N/A	N/A	[41]
0.6% at. Sn-ZnO	3.49	65	3.26	3.4×10^{19}	9.22	8.3×10^{-2}	N/A	N/A	[24]
7% at. Sn-ZnO	0.35	85	3.25	N/A	N/A	N/A	1×10^5	3.5	[42]
1% at. Sn-ZnO	0.3	80	3.25	N/A	N/A	410	37	19.4	[43]
7% at. Sn-ZnO	1	N/A	3.23	10^{21}	5–22	N/A	3105	60	[44]
7% at. Sn-ZnO	0.16	80	3.26	3.9×10^{17}	3	18	2	17	This work

3.4. Sensor Application

Given that the optoelectronic properties of TZO films do not substantially change with the doping percentage, the sensor prototypes were manufactured with 7% Sn-doped ZnO films. This is due, first, to the fact that these films are characterized by low resistivities and high electronic mobility (Figure 5c,d). Second, the currents measured under UV light were the highest, which, from an experimental point of view, is favorable since it avoids complications associated with the instrumental noise present in devices operating at low currents.

The current as a function of time response shown in Figure 7a (black line) illustrates the typical behavior of a sensor that exhibits changes in material resistivity when exposed to electromagnetic radiation in the UV range. These curves are characterized by an increase in current that approaches a linear response, reaching a maximum value, followed by a decrease in current under a negative exponential behavior, as described by the previously explained on/off cycles. On/off response curves were obtained for different values of solar radiation intensity. In laboratory measurements, the use of neutral filters allows the intensity of radiation to be regulated. In field tests, solar intensity was varied depending on daytime hours. The increasing current response curves of the TZO (7%) film exhibited behavior similar to that mentioned in the analysis of monochromatic UV-light response (Figure 6a). The slopes of these curves were calculated for each exposure cycle and plotted, as shown in Figure 7a (red line). The values of these slopes follow a negative exponential behavior, described by the following equation:

$$y = A_0 e^{-x/\tau} + y_0, \quad (3)$$

where the parameter y_0 corresponds to the horizontal asymptote of the slope values of the oxygen desorption response curves on the surface of the TZO (7%) film at long stabilization times of the device. The y_0 parameter for each solar intensity value, both for laboratory and outdoor measurements, shows a linear behavior as a function of solar intensity (Figure 7b).

This indicates that the TZO film responds differently to the same phenomenon under different experimental conditions.

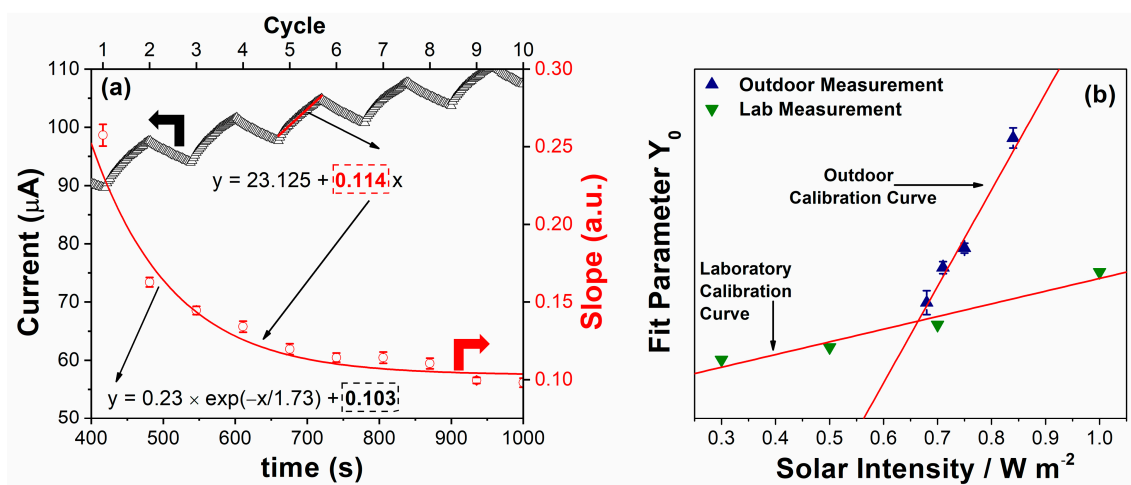


Figure 7. (a) Outdoor current–time response of the sensor (black line) registered at 1 sun of solar radiation and exponential fitting (red curve) of slopes calculated at each response cycle to obtain the sensitivity factor y_0 . (b) Sensitivity curves obtained via linear approximation of the y_0 parameter for outdoor and laboratory measurement of the sensor.

As a thin-film, ZnO offers a high surface-to-volume ratio, which is beneficial for the adsorption and desorption of molecules such as oxygen, which plays a crucial role in the detection mechanism of these sensors. When a UV-sensor based on ZnO is exposed to UV radiation, electron–hole pairs are generated. The free electrons reduce the concentration of adsorbed oxygen on the surface of the ZnO, which decreases the potential barrier at grain boundaries, resulting in an increase in the material’s conductivity [22,37,45]. This change in conductivity allows the sensor to detect the presence of UV radiation. The sensor’s response as a function of UV radiation intensity is influenced by several factors, including the quality of the ZnO thin film, grain size, defect density, and the amount of dopant present in the film (such as the 7% tin-doped TZO). These factors affect both the rate of oxygen adsorption and desorption and the efficiency of the charge carrier generation process under UV radiation. In the context of these sensors described, the analysis of the response curve slopes provides valuable information about the sensor’s response time and stability. The linear behavior of the y_0 parameter as a function of solar intensity indicates good sensor linearity, which is crucial for practical applications requiring precise and reproducible responses to different levels of UV radiation.

Finally, the variability observed in the sensors’ behavior under different experimental conditions highlights the importance of detailed characterization and calibration of UV-sensors in specific operating conditions in order to ensure optimal performance.

4. Conclusions

A simple and low-cost method, namely, as spray pyrolysis, was used to fabricate UV photodetectors based on tin-doped zinc oxide (TZO) films. Structural analysis confirms the polycrystalline character of the films, with a hexagonal structure and single-phase ZnO wurtzite. Although the Sn content in the films was varied significantly, no notable changes in the primary optoelectronic properties were observed. The films showed high sensitivity and photoresponse to ultraviolet light, both monochromatic and that from solar radiation. The results obtained from outdoor measurements at different daytime hours of sunlight showed a promising UV performance sensor using the 7%-Sn-doped ZnO films. The sensor exhibited response to different values of solar radiation with good linearity. These characteristics suggest that the films have significant potential for integration into wearable devices or other technologies for real-time UV monitoring.

Finally, the use of sprayed TZO films could provide a viable solution for the fabrication of UV-sensors with desirable properties such as a wide and direct bandgap, high sensitivity, and ease of fabrication. Furthermore, the cost-effectiveness and simplicity of the spray pyrolysis method make it an attractive option for scalable production, which could facilitate widespread adoption in commercial and industrial applications. The promising results of this study open up new avenues for further optimization and development of TZO-based UV-sensors, particularly in the context of wearable technology and environmental monitoring.

Supplementary Materials: The following supporting information can be downloaded at: <https://www.mdpi.com/article/10.3390/ceramics7040097/s1>, Figure S1: Selected profilometry measurement in TZO films for thickness estimation.

Author Contributions: Conceptualization, M.V. and E.A.V.; investigation, M.V. and E.A.V.; validation, M.V., L.A.R., and R.P.; resources, M.V., E.A.V., and R.P.; writing—original draft preparation, M.V. and E.A.V.; writing—review and editing, M.V., L.A.R., and R.P.; supervision, L.A.R. and R.P.; project administration, L.A.R. and R.P.; funding acquisition, M.V., L.A.R., and R.P. All authors have read and agreed to the published version of the manuscript.

Funding: The authors acknowledge funding support from CONICET (PIP2487), Fondo para la Investigación Científica y Tecnológica ANICYT (I+D FONCYT, project PICT 2425/18; PICT Start up 2021-26) and National University of Mar del Plata (UNMDP, project codes ING667/22; ING693/23 and 15/G577).

Institutional Review Board Statement: Not applicable.

Informed Consent Statement: Not applicable.

Data Availability Statement: The original contributions presented in the study are included in the article/Supplementary Materials, further inquiries can be directed to the corresponding author.

Conflicts of Interest: The authors declare that they have no known competing financial interests or personal relationships that could have appeared to influence the work reported in this paper.

References

1. Ritter, J.W.; Böckmann, C.W. Auszüge aus Briefen an den Herausgeber. *Ann. Phys.* **1801**, *7*, 501–528. [CrossRef]
2. Harm, W. *Biological Effects of Ultraviolet Radiation*; Cambridge University Press: Cambridge, UK, 1980; p. 229.
3. Diffey, B.L. Sources and measurement of ultraviolet radiation. *Methods* **2002**, *28*, 4–13. [CrossRef] [PubMed]
4. Wargent, J.J.; Jordan, B.R. From ozone depletion to agriculture: Understanding the role of UV radiation in sustainable crop production. *New Phytol.* **2013**, *197*, 1058–1076. [CrossRef] [PubMed]
5. Barnes, P.W.; Williamson, C.E.; Lucas, R.M.; Robinson, S.A.; Madronich, S.; Paul, N.D.; Bornman, J.F.; Bais, A.F.; Sulzberger, B.; Wilson, S.R.; et al. Ozone depletion, ultraviolet radiation, climate change and prospects for a sustainable future. *Nat. Sustain.* **2019**, *2*, 569–579. [CrossRef]
6. Huang, X.; Chalmers, A.N. Review of Wearable and Portable Sensors for Monitoring Personal Solar UV Exposure. *Ann. Biomed. Eng.* **2021**, *49*, 964–978. [CrossRef]
7. Wang, J.; Chen, J.; Sun, Y.; He, J.; Zhou, C.; Xia, Q.; Dang, Y.; Pan, D.; Du, L. Ultraviolet-radiation technology for preservation of meat and meat products: Recent advances and future trends. *Food Control* **2023**, *148*, 109684. [CrossRef]
8. Turner, J.; Igoe, D.; Parisi, A.V.; McGonigle, A.J.; Amar, A.; Wainwright, L. A review on the ability of smartphones to detect ultraviolet (UV) radiation and their potential to be used in UV research and for public education purposes. *Sci. Total Environ.* **2020**, *706*, 135873. [CrossRef]
9. Yu, Z.; Xu, J.; Gong, H.; Li, Y.; Li, L.; Wei, Q.; Tang, D. Bioinspired Self-Powered Piezoresistive Sensors for Simultaneous Monitoring of Human Health and Outdoor UV Light Intensity. *ACS Appl. Mater. Inter.* **2022**, *14*, 5101–5111. [CrossRef]
10. Zhou, Y.; Qiu, X.; Wan, Z.A.; Long, Z.; Poddar, S.; Zhang, Q.; Ding, Y.; Chan, C.L.J.; Zhang, D.; Zhou, K.; et al. Halide-exchanged perovskite photodetectors for wearable visible-blind ultraviolet monitoring. *Nano Energy* **2022**, *100*, 107516. [CrossRef]
11. Shur, M. Wide band gap semiconductor technology: State-of-the-art. *Solid State Electron.* **2019**, *155*, 65–75. [CrossRef]
12. Monroy, E.; Omnès, F.; Calle, F. Wide-bandgap semiconductor ultraviolet photodetectors. *Semicond. Sci. Technol.* **2003**, *18*, R33. [CrossRef]
13. BenMoussa, A.; Soltani, A.; Schühle, U.; Haenen, K.; Chong, Y.M.; Zhang, W.J.; Dahal, R.; Lin, J.Y.; Jiang, H.X.; Barkad, H.A.; et al. Recent developments of wide-bandgap semiconductor based UV sensors. *Diam. Related. Mater.* **2009**, *18*, 860–864. [CrossRef]
14. Chen, H.; Liu, K.; Hu, L.; Al-Ghamdi, A.A.; Fang, X. New concept ultraviolet photodetectors. *Mater. Today* **2015**, *18*, 493–502. [CrossRef]

15. Norton, D.P.; Heo, Y.W.; Ivill, M.P.; Ip, K.; Pearton, S.J.; Chisholm, M.F.; Steiner, T. ZnO: Growth, doping & processing. *Mater. Today* **2004**, *7*, 34–40. [[CrossRef](#)]
16. Young, S.-J.; Yang, C.-C.; Lai, L.-T. Review—Growth of Al-, Ga-, and In-Doped ZnO Nanostructures via a Low-Temperature Process and Their Application to Field Emission Devices and Ultraviolet Photosensors. *J. Electrochem. Soc.* **2017**, *164*, B3013. [[CrossRef](#)]
17. Workie, A.B.; Ningsih, H.S.; Shih, S.-J. An comprehensive review on the spray pyrolysis technique: Historical context, operational factors, classifications, and product applications. *J. Anal. Appl. Pyrolysis* **2023**, *170*, 105915. [[CrossRef](#)]
18. Patil, P.S. Versatility of chemical spray pyrolysis technique. *Mater. Chem. Phys.* **1999**, *59*, 185–198. [[CrossRef](#)]
19. International Centre for Diffraction Data (ICCD). *Powder Diffraction File Database*; International Centre for Diffraction Data (ICCD): Newtown Square, PA, USA, 1998.
20. Tauc, J. Optical Properties of Amorphous Semiconductors. In *Amorphous and Liquid Semiconductors*; Tauc, J., Ed.; Springer: Boston, MA, USA, 1974; pp. 159–220.
21. Viezbicke, B.D.; Patel, S.; Davis, B.E.; Birnie, D.P., III. Evaluation of the Tauc method for optical absorption edge determination: ZnO thin films as a model system. *Phys. Status Solidi B* **2015**, *252*, 1700–1710. [[CrossRef](#)]
22. Villegas, E.A.; Aldao, C.M.; Savu, R.; Ramajo, L.A.; Parra, R. Effects of Grain Size on the UV-Photoresponse of Zinc Oxide Thin Films Grown by Spray-Pyrolysis. *Phys. Status Solidi A* **2018**, *215*, 1800107. [[CrossRef](#)]
23. Dedova, T.; Acik, I.O.; Polivtseva, S.; Krunks, M.; Gromyko, I.; Tõnsuaadu, K.; Mere, A. Influence of solution composition on sprayed ZnO nanorods properties and formation process: Thermoanalytical study of the precursors. *Ceram. Int.* **2019**, *45*, 2887–2892. [[CrossRef](#)]
24. Ajili, M.; Castagné, M.; Turki, N.K. Study on the doping effect of Sn-doped ZnO thin films. *Superlattices Microstruc.* **2013**, *53*, 213–222. [[CrossRef](#)]
25. Xu, Z.; Deng, H.; Li, Y.; Cheng, H. Al-doping effects on structure, electrical and optical properties of c-axis-orientated ZnO:Al thin films. *Mater. Sci. Semicond. Process.* **2006**, *9*, 132–135. [[CrossRef](#)]
26. Garcés, F.A.; Budini, N.; Schmidt, J.A.; Arce, R.D. Highly doped ZnO films deposited by spray-pyrolysis. Design parameters for optoelectronic applications. *Thin Solid Films* **2016**, *605*, 149–156. [[CrossRef](#)]
27. Lee, J.-H.; Park, B.-O. Transparent conducting ZnO:Al, In and Sn thin films deposited by the sol-gel method. *Thin Solid Films* **2003**, *426*, 94–99. [[CrossRef](#)]
28. Rousset, J.; Tsin, F.; Guc, M.; Vidal, J.; Le Bris, A.; Thomere, A.; Izquierdo-Roca, V.; Lincot, D. Perchlorate-Induced Doping of Electrodeposited ZnO Films for Optoelectronic Applications. *J. Phys. Chem. C* **2016**, *120*, 18953–18962. [[CrossRef](#)]
29. Berruet, M.; Gau, D.L.; Dalchiele, E.A.; Vázquez, M.; Marotti, R.E. Optical, electrical and structural characterization of chloride-doped ZnO nanopillars obtained by electrodeposition. *J. Phys. D Appl. Phys.* **2016**, *49*, 215103. [[CrossRef](#)]
30. Panda, S.K.; Jacob, C. Preparation of transparent ZnO thin films and their application in UV sensor devices. *Solid State Electron.* **2012**, *73*, 44–50. [[CrossRef](#)]
31. Chahmat, N.; Souier, T.; Mokri, A.; Bououdina, M.; Aida, M.S.; Ghers, M. Structure, microstructure and optical properties of Sn-doped ZnO thin films. *J. Alloys Compd.* **2014**, *593*, 148–153. [[CrossRef](#)]
32. Jain, A.; Sagar, P.; Mehra, R.M. Band gap widening and narrowing in moderately and heavily doped n-ZnO films. *Solid State Electron.* **2006**, *50*, 1420–1424. [[CrossRef](#)]
33. Yung, K.C.; Liem, H.; Choy, H.S. Enhanced redshift of the optical band gap in Sn-doped ZnO free standing films using the sol-gel method. *J. Phys. D Appl. Phys.* **2009**, *42*, 185002. [[CrossRef](#)]
34. Burstein, E. Anomalous Optical Absorption Limit in InSb. *Phys. Rev.* **1954**, *93*, 632–633. [[CrossRef](#)]
35. Kadri, L.; Abderrahmane, A.; Bulai, G.; Carlescu, A.; Doroftei, C.; Motrescu, I.; Gurlui, S.; Leontie, L.; Adnane, M. Optical and Structural Analysis of TiO₂-SiO₂ Nanocomposite Thin Films Fabricated via Pulsed Laser Deposition Technique. *Nanomaterials* **2023**, *13*, 1632. [[CrossRef](#)] [[PubMed](#)]
36. Rousset, J.; Saucedo, E.; Lincot, D. Extrinsic Doping of Electrodeposited Zinc Oxide Films by Chlorine for Transparent Conductive Oxide Applications. *Chem. Mater.* **2009**, *21*, 534–540. [[CrossRef](#)]
37. Villegas, E.A.; Ramajo, L.A.; Lere, M.E.; Castro, M.S.; Parra, R. UV-response of aluminum-doped zinc oxide transparent films with different microstructures and electrical properties. *Mater. Sci. Semicond. Process.* **2021**, *121*, 105412. [[CrossRef](#)]
38. Ahn, S.E.; Lee, J.S.; Kim, H.; Kim, S.; Kang, B.H.; Kim, K.H.; Kim, G.T. Photoresponse of sol-gel-synthesized ZnO nanorods. *Appl. Phys. Lett.* **2004**, *84*, 5022–5024. [[CrossRef](#)]
39. Law, J.B.K.; Thong, J.T.L. Simple fabrication of a ZnO nanowire photodetector with a fast photoresponse time. *Appl. Phys. Lett.* **2006**, *88*, 133114. [[CrossRef](#)]
40. Hu, L.; Zhu, L.; He, H.; Guo, Y.; Pan, G.; Jiang, J.; Jin, Y.; Sun, L.; Ye, Z. Colloidal chemically fabricated ZnO:Cu-based photodetector with extended UV-visible detection waveband. *Nanoscale* **2013**, *5*, 9577–9581. [[CrossRef](#)]
41. Shelke, V.; Sonawane, B.K.; Bhole, M.P.; Patil, D.S. Electrical and optical properties of transparent conducting tin doped ZnO thin films. *J. Mater. Sci. Mater. Electron.* **2012**, *23*, 451–456. [[CrossRef](#)]
42. Kumar, M.; Bhatt, V.; Abhyankar, A.C.; Kim, J.; Kumar, A.; Yun, J.-H. Modulation of structural properties of Sn doped ZnO for UV photoconductors. *Sens. Actuators A* **2018**, *270*, 118–126. [[CrossRef](#)]
43. Aslan, E.; Zarbali, M. Tuning of photosensitivity and optical parameters of ZnO based photodetectors by co-Sn and Ti doping. *Opt. Mater.* **2022**, *125*, 112030. [[CrossRef](#)]

44. Pujar, S.M.; Bhat, S.; Rao, G.K.; Mahesha. Reduced Persistent Photoconductivity in Successive Ionic Layer Adsorption and Reaction-Deposited ZnO:Sn Thin Films. *Phys. Status Solidi A* **2024**, 2400451. [[CrossRef](#)]
45. Ning, Y.; Zhang, Z.; Teng, F.; Fang, X. Novel Transparent and Self-Powered UV Photodetector Based on Crossed ZnO Nanofiber Array Homojunction. *Small* **2018**, *14*, 1703754. [[CrossRef](#)] [[PubMed](#)]

Disclaimer/Publisher's Note: The statements, opinions and data contained in all publications are solely those of the individual author(s) and contributor(s) and not of MDPI and/or the editor(s). MDPI and/or the editor(s) disclaim responsibility for any injury to people or property resulting from any ideas, methods, instructions or products referred to in the content.